ACTA IMEKO
ISSN: 2221-870X
December 2023, Volume 12, Number 4, 1 - 6

Image uncertainty components in video strain measurement of mortar destructive compression testing

Luís Lages Martins[1], Ana Isabel Marques[1], Álvaro Silva Ribeiro[1]

[1] *LNEC – National Laboratory for Civil Engineering, Avenida do Brasil 101, 1700-066 Lisboa, Portugal*

ABSTRACT
This paper describes a video strain measurement solution developed for application in mortar destructive compression testing. Knowledge about the mechanical behavior of this type of construction material, namely up to its fracture, is still superficial due to the less common use of non-contact measurement methods. The performed research was focused on the determination of image coordinate accuracy, based on the experimental quantification of the identified main uncertainty components, using traceable reference patterns, and validated computational toolboxes dedicated to camera parameterization and digital image processing. The obtained results show the following uncertainty contributions: lens distortion - negligible; re-projection errors - 0.21 pixel; 0.10 pixel - spatial resolution; and digital image processing operations - 0.28 pixel. The combination of these uncertainty components resulted in an image coordinate standard uncertainty equal to 0.36 pixel, which was propagated (in addition to the scale coefficient measurement uncertainty) to the selected camera model – orthographic projection with uniform scaling – which supports the video strain measurement.

Section: RESEARCH PAPER

Keywords: Video strain measurement; measurement uncertainty; mortar; compression testing

Citation: Luís Lages Martins, Ana Isabel Marques, Álvaro Silva Ribeiro, Image uncertainty components in video strain measurement of mortar destructive compression testing, Acta IMEKO, vol. 12, no. 4, article 30, December 2023, identifier: IMEKO-ACTA-12 (2023)-04-30

Section Editor: Eric Benoit, Université Savoie Mont Blanc, France

Received July 5, 2022; **In final form** December 11, 2023; **Published** December 2023

Funding: This work was supported by the Portuguese National Laboratory for Civil Engineering.

Corresponding author: Luís Lages Martins, e-mail: lfmartins@lnec.pt

1. INTRODUCTION

Construction materials research have an important contribution for the development of innovative products and solutions aiming the improvement of structural safety, energy efficiency, comfort, and architecture of buildings.

Mortars, which can be used as bedding mortar in masonry and as coatings in buildings, play an important role in wall strengthening, water protection, thermal and acoustic insulation and, also, in terms of aesthetic. They have been applied in building construction since ancient times and are widely used still today as a construction material in buildings.

The common presence of mortars in historical buildings fully justifies conducting research studies aiming the characterization of their mechanical behaviour, having as main objectives the heritage preservation and the reduction of the seismic vulnerability of this type of buildings [1]-[3]. Whenever it is necessary to apply reinforcement solutions, and it is not possible to keep the original coating mortars, the use of reinforced renders or plasters with meshes or fibres is often chosen, considering the architectural limitations of historic buildings. For the development of this type of reinforcement solutions, and compatibility assessment between the new and original materials, the destructive compressive strength test of mortar specimens is often used in the experimental study of different types of mortar compositions and reinforcement materials. In this type of testing, two quantities are simultaneously measured: the uniaxial compression force and the specimen strain in both the vertical and transverse directions [4]. With these quantities it is possible to determine two fundamental characteristics: the static modulus of elasticity and the Poisson's ratio, which support in the decision to choose the type of reinforcement mortars compatible with existing mortars and are essential data for the numerical models used in the design of the most suitable reinforcement solution.

From a conventional point of view, strain measurement is performed with contact extensometers using several configurations and apparatus. In more recent years, new non-contact extensometry technologies have emerged, namely, using

laser and video measurement solutions [5]-[7]. Within this last category, several measurement techniques are available such as digital image correlation (DIC) [8], electronic speckle-pattern interferometry (ESPI) [9], photoelasticity [10], geometric moiré [11] and grating interferometry [12].

Although non-contact strain measurement methods are recommended for material destructive testing (due to the low instrumental damage risk) [13], knowledge about measurement models, uncertainty components and their propagation from input to output quantities is still limited.

The aim of this study was the quantification of the image uncertainty components related to the video strain measurement in mortar specimens subjected to destructive compression testing. This knowledge is a key issue for the measurement uncertainty propagation to the strain quantity and other mechanical quantities – elasticity modulus, Poisson ratio and others – which support the mechanical characterization of mortars applied in buildings.

This paper describes, in Section 2, the used video strain measurement approach, based in an orthographic camera model. Section 3 mentions the experimental methods applied in the quantification of image uncertainty components such as distortion, re-projection errors, spatial resolution, and digital image processing. The obtained results are presented in Section 4, while Section 5 reports the conclusions obtained from the performed study.

2. VIDEO STRAIN MEASUREMENT APPROACH

The selection of a non-contact strain measurement approach was justified by the interest of determining the mortar specimen mechanical behaviour near its fracture, avoiding the high risk of damaging the instrumental apparatus, as it would be the case if contact extensometers were used for strain measurement. The use of the testing compression machine dimensional measurement chain was not considered a suitable solution since: (i) it is restricted to the specimen's vertical deformation measurement (therefore, the determination of the Poisson's ratio is not possible), and (ii) differences can arise between local (specimen) and global (machine components) deformations.

Within the set of available non-contact measurement solutions, video strain measurement was considered a reasonable solution from an economic point of view, if the target measurement uncertainty (in this case, 0.01 mm, considering a confidence interval of 95 %) is achievable, justifying the study described in this paper.

The selected measurement approach was supported in the orthographic camera model [14], where a parallel relation between the image plane and the specimen's front plane is assumed (as shown in Figure 1). By adopting this camera model, special attention must be given to the positioning and orientation of the camera in the observation scenario relative to the specimen under compression testing, to assure the mentioned geometrical relation between planes. A uniform scaling between the image (x, y) and specimen (X, Y) coordinates was considered, being expressed by:

$$\begin{bmatrix} X \\ Y \end{bmatrix} = K \begin{bmatrix} x \\ y \end{bmatrix}, \tag{1}$$

where K is the scale coefficient (in mm·pixel^{-1}) which converts the image coordinates (in pixel) to specimen coordinates (in mm).

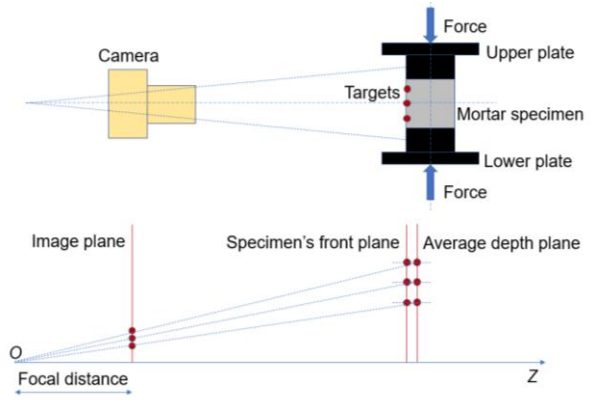

Figure 1. Adopted camera model.

Since a high spatial resolution of the acquired images contributes for the measurement accuracy, in this study, the digital camera was placed near the specimen under compression (with an observation distance close to 500 mm) and the focal distance, f, (between 28 mm and 300 mm) was manually adjusted to assure a suitable field-of-view (all targets and reference dimensions visible in the image) and focusing (to avoid the blurring effect in interest objects). Therefore, the effect of the camera lens distortion must be studied. In this work, Brown's distortion model [15] was applied, being composed by two main components: radial and tangential distortions. In this model, the functional relation between distorted image coordinates (x_p, y_p) and undistorted image coordinates (x_d, y_d) is given by:

$$\begin{bmatrix} x_d \\ y_d \end{bmatrix} = \begin{bmatrix} 1 + k_1 \cdot r^2 + k_2 \cdot r^4 + k_5 \cdot r^6 \\ 1 + k_1 \cdot r^2 + k_2 \cdot r^4 + k_5 \cdot r^6 \end{bmatrix} + \begin{bmatrix} 2 \cdot k_3 \cdot x_p \cdot y_p + k_4 \cdot \left(r^2 + 2 \cdot x_p^2\right) \\ k_3 \cdot \left(r^2 + 2 \cdot y_p^2\right) + 2 \cdot k_4 \cdot x_p \cdot y_p \end{bmatrix}, \tag{2}$$

where k_1, k_2, and k_5 are the radial distortion coefficients and k_3, and k_4 are the tangential distortion coefficients, and r^2 is an auxiliary variable defined by

$$r^2 = x_p^2 + y_p^2 . \tag{3}$$

The quantification of the scale coefficient was supported in traceable dimensions observed in the field-of-view, namely, in the specimen and compression plates, as shown in Figure 2.

A mesh of nine passive targets was placed in the central region of the front surface of the tested mortar specimen, as shown in Figure 3, to measure the vertical and the transverse strains between points.

Table 1 summarizes the main experimental setup components and the corresponding specifications.

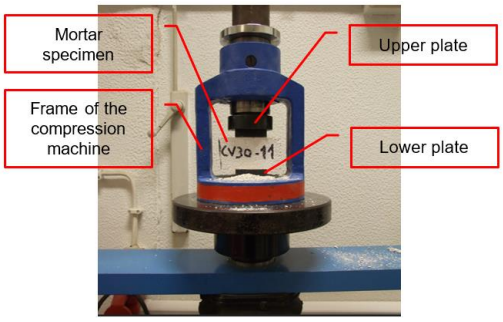

Figure 2. Mortar testing apparatus.

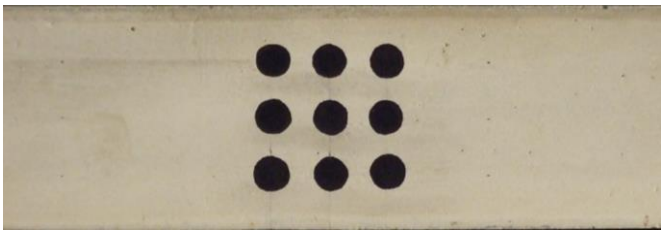

Figure 3. Passive targets on the mortar specimen's front plane.

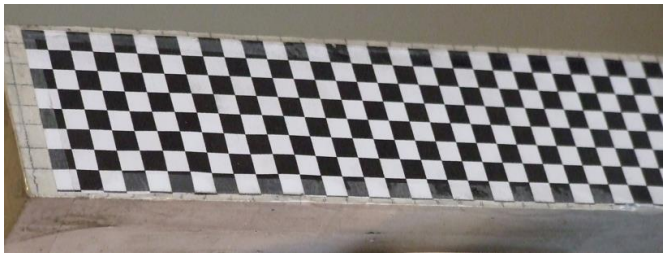

Figure 4. Example of acquired image for the lens distortion study.

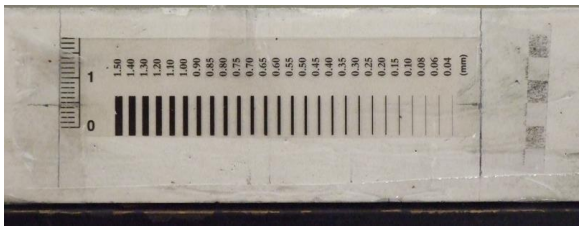

Figure 5. Reference pattern in mortar specimen.

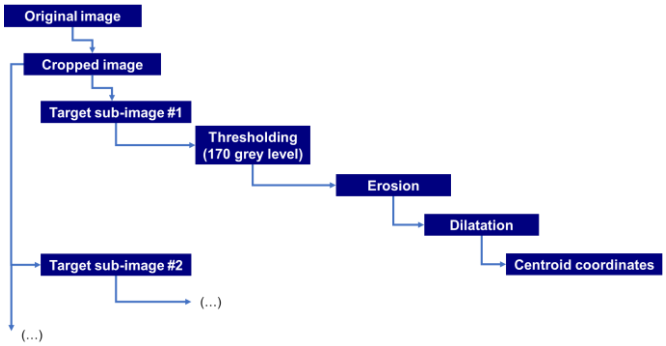

Figure 6. Applied digital image processing.

3. QUANTIFICATION OF IMAGE UNCERTAINTY COMPONENTS

3.1. Distortion

In this study, the quantification of the image uncertainty component related to the lens distortion was performed using a dedicated toolbox [16]. A total of 15 images were collected in the observation scenario, i.e. mortar specimen placed in the compression plates of the testing machine. A chessboard pattern (see Figure 4), with a nominal linear square dimension of 4.5 mm, was placed in the front surface of the mortar specimen (dimensions of 40 mm × 40 mm × 160 mm), being its position and orientation manually changed between image acquisitions and fixed in the experimental apparatus.

3.2. Re-projection errors

This image uncertainty component is related to the study of the lens distortion, described in Section 3.1. Although the camera model (pinhole model) [14] adopted in the toolbox [16] is more accurate than the orthographic camera model, the quantification of the distortion coefficients (and other optional intrinsic and extrinsic camera parameters) is influenced by the uncertainty contributions emerging from the image digital extraction process of the reference points in the pattern and the non-linear optimization calculation procedure (iterative gradient descend with an explicit – close-form – computation of the Jacobian matrix) [16]. Based on the obtained camera parameters, the image reference points can be re-projected on the used images and the dispersion of values related to the differences between points (original and re-projected) can be used to assess the accuracy of the parametrization process.

3.3. Spatial resolution

The image space resolution was studied using a pattern placed in the front surface of a mortar specimen in testing position. The pattern – composed by traceable lines of different width (from 0.04 mm up to 1.50 mm) – was orientated in the transverse testing direction and one image was acquired (shown in Figure 5). In this case, the pattern was kept in the same position and orientation during the image acquisition.

3.4. Digital image processing

The determination of image coordinates related to points of interest in the specimen was performed using a dedicated computational routine developed in Matlab, composed by the following main steps (shown in Figure 6): (i) original image cropping; (ii) generation of individual target sub-image; (iii) thresholding operation (170 grey level) for binary sub-image generation; (iv) morphological operations (erosion and dilatation); and (v) target centroid determination.

The dispersion of differences between target image coordinates, related to the variation of the processing parameters, was studied and quantified.

4. RESULTS

4.1. Distortion

The acquired chessboard pattern images were used in [16] for the estimation of the camera intrinsic parameters, namely, to evaluate the lens distortion coefficients. To reduce the computational effort, the centre of the collected images was assumed as the camera principal point (x_0, y_0), the pixel skew was

Table 1. Specifications of the experimental setup components.

Component	Brand and model	Specifications
Digital camera	Fujifilm / FinePix S6500fd	1/17'' CCD sensor; 6.3 megapixels
Optical lens	Fujinon	Optical zoom 10.7×; aperture F2.8 – F4.9; focal distance 28 mm – 300 mm (35 mm equivalent)
Tripod	Manfrotto / MKBFRLA4BK-BH	Dimension: 128 cm - 151 cm (opened); 40 cm (closed); mass 1.59 kg

Table 2. Probabilistic formulation of the input quantities for the Monte Carlo simulation.

Input quantity	Symbol	Estimate	Probability distribution	Standard uncertainty
Focal distance	f	13525 pixels	Gaussian	36 pixels
Principal point x coordinate	x_0	400 pixels	Gaussian	0 pixel
Principal point y coordinate	y_0	400 pixels	Gaussian	0 pixel
1st radial distortion coefficient	k_1	$13.9 \cdot 10^{-14}$ pixel^{-2}	Gaussian	$1.9 \cdot 10^{-14}$ pixel^{-2}
2nd radial distortion coefficient	k_2	$-38.9 \cdot 10^{-21}$ pixel^{-4}	Gaussian	$2.9 \cdot 10^{-21}$ pixel^{-4}
1st tangential distortion coefficient	k_3	$12.2 \cdot 10^{-11}$ pixel^{-1}	Gaussian	$1.4 \cdot 10^{-11}$ pixel^{-1}
2nd tangential distortion coefficient	k_4	$16.9 \cdot 10^{-12}$ pixel^{-1}	Gaussian	$2.0 \cdot 10^{-12}$ pixel^{-1}

considered negligible as well as the last order radial distortion coefficient (k_5).

The obtained probabilistic information (shown in Table 2) was used in Monte Carlo numerical simulation [17] for the quantification of lens distortion impact in the accuracy of the image coordinates, considering the mathematical models given by expressions (2) and (3).

Figure 7 and Figure 8 show, respectively, the measurement estimates and expanded uncertainties of the combined effect of radial and tangential distortions in the accuracy of the image coordinates for a sub-image with a dimension of 800 × 800 pixels.

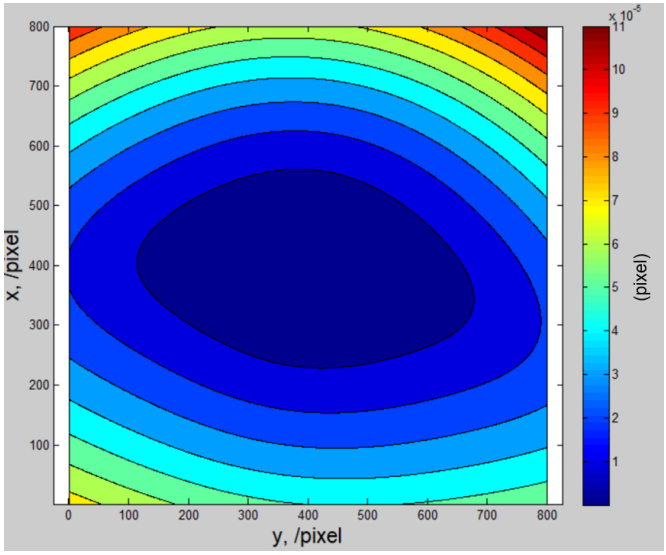

Figure 7. Estimates of the impact of the lens distortion (in pixel).

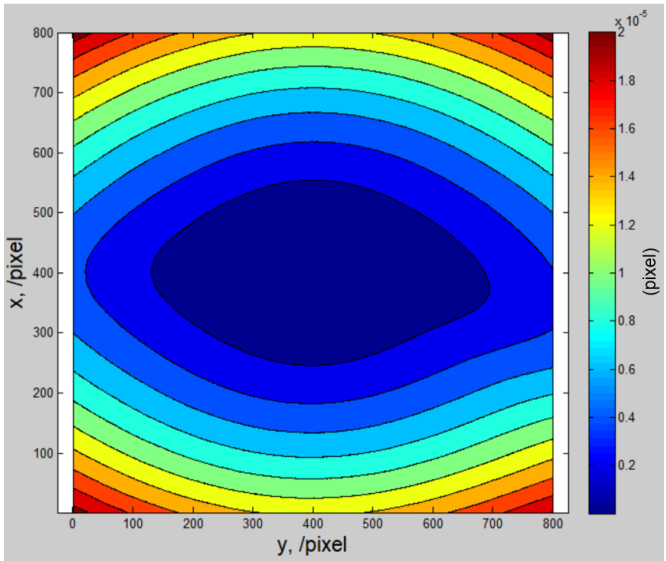

Figure 8. Expanded uncertainties (95 % confidence interval) of the impact of the lens distortion (in pixel).

The obtained results show a negligible impact of the lens distortion in the accuracy of the image coordinates (lower than $1.19 \cdot 10^{-4}$ pixel, for the extreme regions of the sub-image). The maximum expanded measurement uncertainty was equal to $0.21 \cdot 10^{-4}$ pixel. The reduced impact of the lens distortion is justified by the image partial spatial analysis of its central region (800 × 800 pixels, i.e., the dimension of the interest field-of-view), instead of the image full field-of-view (2848 × 2136 pixels). In addition, the use of an intermediate focal distance and a macro image acquisition mode were also used.

4.2. Re-projection errors

The dispersion of values related to the re-projection errors was obtained from [16] in the quantification of the lens distortion coefficients (mentioned in Section 4.1), being shown in Figure 9.

Assuming a Gaussian probability density function, a standard uncertainty equal to 0.21 pixel was assigned to the re-projection error uncertainty component.

4.3. Spatial resolution

Figure 10 shows the relation obtained between the reference width of the markings in the observed pattern and the corresponding number of pixels, for the case of the transverse direction.

Considering the results achieved and an interpolation of 1/10 of a pixel in the digital image processing, the metric spatial resolution corresponded, approximately, to 3.8 μm.

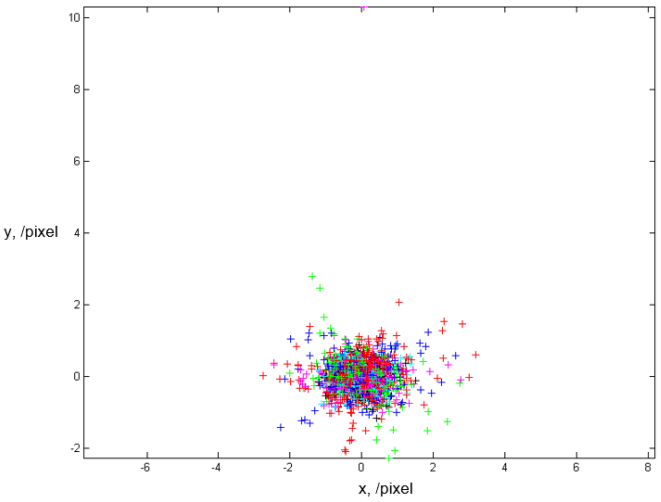

Figure 9. Dispersion of re-projection errors in the acquired images (individual colour marking for each image).

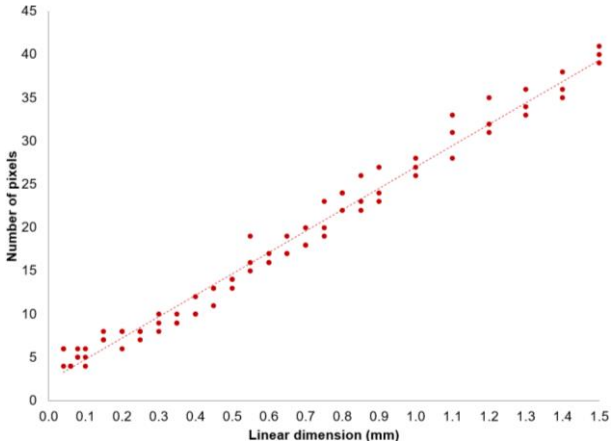

Figure 10. Determination of the image spatial resolution.

4.4. Digital image processing

The grey level histogram of the targets sub-images showed two frequency peaks (close to 34 and 189 grey levels) which supported the thresholding operation, allowing the generation of a binary image of the individual targets and their surroundings. In addition, the dimension of the structural element (disk type) for the morphological operations was also set to a value of 10 pixels, based on the visual analysis of the corresponding the targets binary images. Changes in these two digital image processing parameters (threshold value between 80 and 170 grey levels, and structural element dimension between 5 and 10 pixels) were introduced in the routine and the corresponding impact was evaluated in the obtained target image coordinates, revealing a standard uncertainty of 0.28 pixel.

4.5. Measurement uncertainty evaluation

Based on the quantification of the image uncertainty components described in the previous Sections (4.1 to 4.4), the combined measurement uncertainty of the image coordinates, $u(x,y)$, can be obtained from the application of the Law of Propagation of Uncertainty (LPU) [17]:

$$u(x,y) = \sqrt{u^2(x,y)_{\text{dist}} + u^2(x,y)_{\text{reproj}} + u^2(x,y)_{\text{res}} + u^2(x,y)_{\text{dip}}}\,, \tag{4}$$

where $u(x,y)_{\text{dist}}$ is the distortion uncertainty component (see Section 4.1), $u(x,y)_{\text{reproj}}$ is the re-projection error uncertainty component (studied in Section 4.2), $u(x,y)_{\text{res}}$ is the spatial resolution uncertainty component (quantified in Section 4.3) and $u(x,y)_{\text{dip}}$ is the digital image processing uncertainty component (discussed in Section 4.4). An image coordinate standard uncertainty equal to 0.36 pixel was obtained in the studied case.

The obtained measurement uncertainty was propagated to the output quantity – specimen coordinates (X, Y), considering the additional measurement uncertainty related to the input quantity scale coefficient, K, as represented in functional diagram shown in Figure 11.

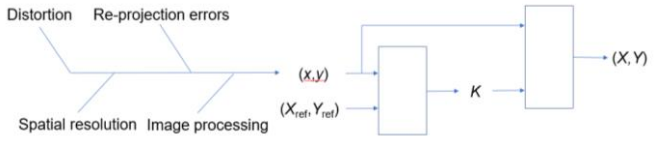

Figure 11. Measurement uncertainty propagation from input to output quantities.

Table 3. Scale coefficient estimate and standard uncertainty and corresponding input quantities (metric and pixel values of the reference line)

Reference line width (mm)	Image dimension (pixel)	Scale coefficient (mm·pixel^{-1})
1.4843 ± 0.0031	39.66 ± 0.36	0.03806 ± 0.00035

According to the selected measurement approach, the scale coefficient (an intermediate quantity) was estimated from the linear relation between in reference dimensions (X_{ref}, Y_{ref}) previously measured (in the specimen or compression plates, for example) and visible in the camera's field-of-view, and the corresponding image coordinates (with a standard uncertainty of 0.36 pixel previously quantified), i.e.

$$K = \left[\frac{X_{\text{ref}}}{x} \quad \frac{Y_{\text{ref}}}{y}\right]. \tag{5}$$

In this case, the application of the LPU [17] results in the following expression

$$u(K) = \sqrt{\left(\frac{1}{x}\right)^2 \cdot u^2(X_{\text{ref}}) + \left(-\frac{X_{\text{ref}}}{x^2}\right)^2 \cdot u^2(x)}, \tag{6}$$

or, alternatively,

$$u(K) = \sqrt{\left(\frac{1}{y}\right)^2 \cdot u^2(Y_{\text{ref}}) + \left(-\frac{Y_{\text{ref}}}{y^2}\right)^2 \cdot u^2(y)}. \tag{7}$$

The image collected for the study of the spatial resolution (see Figure 5 in Section 3.3) was used for the scale coefficient estimation. Measurement estimates and uncertainties related to the line width in the reference pattern were determined using an SI traceable optical measurement machine. Table 3 shows the scale coefficient estimate and standard uncertainty.

Considering the selected camera model, given by expression (1), the LPU [17] provides the following expressions for the dimensional standard uncertainty:

$$u(X) = \sqrt{K^2 \cdot u^2(x) + x^2 \cdot u^2(K)}\,, \tag{8}$$

or, alternatively,

$$u(Y) = \sqrt{K^2 \cdot u^2(y) + y^2 \cdot u^2(K)}\,. \tag{9}$$

The application of the probabilistic information regarding the standard measurement uncertainties of the scale coefficient and image coordinates, allowed the quantification of the corresponding dimensional standard uncertainty, for the expected dimensional measurement interval (from 0 mm up to 1.5 mm) in mortar destructive testing.

The obtained standard uncertainties varied between 0.013 mm (for estimates close to zero) up to 0.019 mm (near a 1.5 mm dimensional measurement). These values are slightly above the usual measurement resolution (equal to 0.01 mm) of testing compression machine dimensional measurement chains.

5. CONCLUSIONS

The combination of the studied image uncertainty components, by application of the LPU, showed that estimates of target image coordinates can be obtained with an accuracy level close to 0.36 pixel.

The major contribution for this value is related to the digital image processing, followed by the re-projection errors and the spatial resolution.

The obtained measurement uncertainty was propagated, in an intermediate stage, through the scale coefficient model considering the remaining measurement uncertainty related to the reference dimension. In a final stage, this uncertainty knowledge was also being propagated through the orthographic camera model with uniform scaling. The obtained dimensional standard uncertainty (between 0.013 mm and 0.019 mm) is now available for propagation to the strain quantity and, subsequently, to the mechanical quantities of interest in the mortar destructive compression testing. In the specific case of the Poisson's ratio, correlation effects must also be studied since the same video strain measurement approach is used for both vertical and transverse directions.

Future work will also focus on the experimental implementation of the proposed video strain measurement in mortar destructive compression testing, namely, in the development of: (i) the instrumental synchronization process between different measurement chains (force and strain quantities) and; (ii) the digital image processing routine dedicated to the extraction of individual images from destructive testing recorded videos.

ACKNOWLEDGEMENT

The authors are grateful to the Portuguese National Laboratory for Civil Engineering (LNEC), for the financial support, namely, to the LNEC's Scientific Instrumentation Centre and the Buildings Department.

REFERENCES

[1] U. Tomassetti, A. Correia, F. Graziotti, A. Marques, M. Mandirola, P. Candeias, Collapse Shaking Table Test on a URM Cavity Wall Building Representative of a Dutch Terraced House, Eucentre Research Report, Eucentre, Pavia, 2017.

[2] A. Correia, A. Marques, V. Bernardo, L. Grottoli, U. Tomassetti, F. Graziotti, Shake Table Test up to Collapse on a Roof Substructure of a Dutch Terraced House, Eucentre Research Report, Eucentre, Pavia, 2017.

[3] S. Kallioras, A. Correia, A. Marques, V. Bernardo, P. Candeias, F. Graziotti, LNEC-Build-3: An Incremental Shake-Table on a Dutch URM Detached House with Chimneys, Eucentre Research Report EUC203/2018U, Eurocentre, Pavia, 2018.

[4] A. Marques, J. Ferreira, P. Candeias, R. Veiga, Axial Compression and Bending Tests on Old Masonry Walls, Proc. of the 3rd Int. Conf. on Protection of Historical Constructions, Lisbon, Portugal, 12-15 July 2017.

[5] D. Corr, M. Accardi, L. Graham-Brady, S. Shah, Digital Image Correlation Analysis of Interfacial Debonding Properties and Fracture Behavior in Concrete, Eng. Fract. Mech., 74 (2007), Issues 1-2, pp. 119-127. DOI: 10.1016/j.engfracmech.2006.01.035

[6] M. Tekieli, S. De Santis, G. Felice, A. Kwiecien, F. Roscini, Application of Digital Image Correlation to Composite Reinforcements Testing, Compos. Struct, 160 (2017), pp. 670-688. DOI: 10.1016/j.compstruct.2016.10.096

[7] C. Caggigi, D. Sciuto, M. Cuomo, Experimental Study on Effective Bond Length of Basalt Textile Reinforced Mortar Strengthening System: Contributions of Digital Image Correlation, Measurement 129 (2018), pp. 119-127. DOI: 10.1016/j.measurement.2018.07.003

[8] N. McCormick, J. Lord, Digital Image Correlation, Materials Today 13 (2010), pp. 52-54. DOI: 10.1016/S1369-7021(10)70235-2

[9] O. J. Lokberg, G. Slettemoen, Applied Optics and Optical Engineering, J. C. Wyant, R. Shannon (editors), Academic Press, New York, 1987.

[10] A. Kuske, G. Robertson, Photoelastic Stress Analysis, Wiley, London, 1974.

[11] D. Post, Developments in Moiré Interferometry, Opt. Engineering, 21 (1982), pp. 458-467. DOI: 10.1117/12.7972930

[12] K. J. Gasvik, M. E. Fourney, Projection Moire using Digital Video Processing: a Technique for Improving the Accuracy and Sensitivity, J. Appl. Mech, 53 (1986), pp. 652-656. DOI: 10.1115/1.3171826

[13] L. Martins, A. Marques, A. Ribeiro, P. Candeias, M. Veiga, J. Ferreira, Optical Measurement of Planar Deformations in Destructive Mechanical Testing of Masonry Specimens, Appl. Sci. 10, 371 (2020), pp. 1-24. DOI: 10.3390/app10010371

[14] R. Hartley, A. Zisserman, Multiple View Geometry in Computer Vision, 2nd edition, Cambridge University Press, 2005.

[15] D. Brown, Close Range Camera Calibration, Photogrammetry Engineering (1971), pp. 855-866.

[16] J. Bouguet, Camera Calibration Toolbox for Matlab. Online [Accessed 18 July 2023]. http://robots.stanford.edu/cs223b04/JeanYvesCalib/index.html

[17] JCGM 101:2008 – Evaluation of measurement data – Supplement 1 to the "Guide to the expression of uncertainty in measurement" – Propagation of distributions using a Monte Carlo method, 1st edition, JCGM – Joint Committee for Guides in Metrology, 2008

[18] JCGM 100:2008 (GUM 1995 with minor corrections) – Evaluation of measurement data – Guide to the expression of uncertainty in measurement, 1st edition, JCGM – Joint Committee for Guides in Metrology), September 2008.